Ultrasonics Sonochemistry 130 (2026) 107911

Contents lists available at ScienceDirect

Ultrasonics Sonochemistry

journal homepage: www.elsevier.com/locate/ultson

Probing radiation forces acting on acoustic bubbles using digital in-line holography

Cyril Mauger [a,*], Claude Inserra [b], Antoine Lotton [a,b], Nathalie Grosjean [a], Alexander A. Doinikov [a,b], Philippe Blanc-Benon [a], Loïc Méès [a]

[a] INSA Lyon, CNRS, Ecole Centrale de Lyon, Universite Claude Bernard Lyon 1, LMFA, UMR5509, 69621 Villeurbanne, France
[b] Université Claude Bernard Lyon 1, Centre Léon Bérard, INSERM, LabTAU, F-69003 Lyon, France

ARTICLE INFO

Keywords:
Digital in-line holography
Microbubble
Cavitation
Ultrasound

ABSTRACT

A digital in-line holography technique (DIH) is applied to measure non-invasively the three-dimensional motion of micrometric bubbles in an acoustic field. In addition to the components of the bubble displacements, DIH also allows the measurement of the temporal evolution of the bubble radii. It is shown that the knowledge of these four variables allow assessing the various forces that the bubbles experience. In the absence of the acoustic field, the buoyancy and drag forces are assessed. When the acoustic field is switched on, the primary radiation force acting on a single bubble is quantified. The order of the magnitude of the force, as well as its evolution along the bubble trajectory, are captured. It is demonstrated that the location of pressure nodes and antinodes in the cavity are recovered when compared with numerical simulations of the acoustic pressure field. When two bubbles nucleated in the cavity are investigated, they can attract and coalesce under the action of the secondary radiation force. DIH technique allows the quantification of this attractive force acting between the bubbles. The evolution of the secondary Bjerknes force with the interbubble distance is shown to be consistent with theoretical models.

1. Introduction

Acoustic cavitation occurs when a sound field of sufficiently high amplitude allows rupturing a liquid, a phenomenon resulting in the nucleation and activities of gas bubbles [1]. Acoustic bubbly flows are frequently encountered in engineering problems, such as ultrasonic cleaning [2] and sonochemistry [3], but also in biomedicine where the use of acoustic bubbles is a very promising area of research. Amongst the potential health applications, one can mention the destruction of blood clots (sonothrombolysis [4]), the targeted drug delivery into biological materials [5], the bubble-induced opening of the blood–brain barrier for the treatment of brain tumors and neurodegenerative diseases [6,7], or the disinfection of sensitive surfaces (like the skin or vegetables) [8]. In all these disciplines and related technologies, bubbles usually do not appear isolated, but rather in the form of a group of several bubbles. These bubbles are scarcely dispersed homogeneously, but instead self-organize into structured ensembles called a bubble cloud [9]. The understanding of the emergence and spatiotemporal dynamics of these clouds is quite challenging, due to the numerous complex phenomena acting at the scale of a single bubble and between them. Usually, the physics of a huge number of coupled nonlinear oscillators is tackled using numerical modeling based on a continuum approach of the bubbly liquid [10]. The important parameters in the characterization of multibubble cavitation fields are the size distribution of bubbles and their locations in the acoustic field. The knowledge of these two quantities allows assessing the different forces acting on each bubble, as well as the strength of the bubble interaction. Therefore, the size and dynamics of the cloud can be predicted over time.

The size of acoustic cavitation bubbles is usually difficult to predict due to the stochastic process of bubble nucleation and cavitation. Once nucleated, the size distribution of cavitating bubbles can evolve along with the various physical effects that each bubble can encounter in a sound field: coalescence between bubbles [11,12], fragmentation into several daughter bubbles [13,14], growth or shrinking due to rectified diffusion [15,16]. Various techniques have been designed for the measurement of the size distribution of gas bubbles in a liquid including laser light diffraction and phase-Doppler techniques [17], the evolution of the void rate using electromagnetic methods [18,19], the estimation of the bubble dissolution time [20] or the acoustic monitoring of the scattering intensity of the bubble cloud [21,22]. All these techniques

* Corresponding author.
E-mail address: cyril.mauger@insa-lyon.fr (C. Mauger).

https://doi.org/10.1016/j.ultsonch.2026.107911
Received 26 March 2026; Received in revised form 16 May 2026; Accepted 1 June 2026
Available online 5 June 2026

provide reliable results on the overall size distribution of an ensemble of bubbles, whatever the bubble concentration, but do not allow the quantification of the bubble location nor the forces acting on them. Moreover, usually their time resolution is low, so that the temporal evolution of the bubble size distribution is captured at timescale much larger than the acoustic period.

The experimental characterization of the spatial organization of cavitating bubbles is a challenging task. The spatial dynamics of a bubble cloud is qualitatively captured by high-speed imaging, for a description of its macroscopic features [23–25]. The main limitations of these conventional imaging techniques are the lack of details on the individual bubble behaviors and locations, and that they do not allow resolving the three-dimensional nature of the cavitation field. High-speed X-ray phase contrast imaging overcomes these limitations and has been used to investigate the onset of cavitation bubbles induced by an ultrasonic horn [26]. However, this technique is from being accessible for conventional laboratory use. Digital in-line holography (DIH) [27,28] is a technique relying on the numerical reconstruction of holograms (the interference of the coherent light scattered from particles with the incident beam) located at various depths into focus. It enables the simultaneous measurement of the particle size and spatial distribution, and has been widely used in the characterization of the evaporating droplet processes [29,30] and the study of fast-moving bubbles in mixture flows [31]. In the field of ultrasound cavitation, the volumetric oscillations of bubble clouds induced by high-intensity focused ultrasound beam was investigated by high-speed DIH [32], and the motion of individual bubbles was resolved but not discussed so far.

When considering a single bubble, the knowledge of both its size and location as a function of time, and so its velocity and acceleration, provides a way to assess the different forces acting on it. In addition to the added mass, drag and buoyancy forces, gas bubbles in a sound field are submitted to radiative forces, known as the primary and secondary Bjerknes forces [33]. These forces take their origin in the coupling of the volumetric bubble oscillations $V_i(t)$ (where the index i runs for the N bubbles in the cloud) with the spatial pressure gradient, that produces a net force $\mathbf{F_{R,i}} = -\langle V_i(t)\nabla p(\mathbf{r_i}, t)\rangle$, where $\mathbf{r_i}$ is the position vector of the ith bubble and the subscript R stands for the radiative effect. When the pressure gradient comes from the acoustic field itself, the force $\mathbf{F_{R1}}$ is called the primary radiation force. When the pressure gradient is brought by a second neighboring bubble, the force $\mathbf{F_{R2}}$ is called the secondary radiation force. The primary Bjerknes force is responsible for the trapping of gas bubbles at nodes or antinodes of the ultrasound field [34,35], while the secondary Bjerknes force dictates the translational motion of interacting bubbles, giving to the bubble clouds their peculiar spatial organization [23]. The translational motion of each individual bubble i in the cloud is then described by

$$\mathbf{F_{M,i}} + \mathbf{F_{B,i}} + \mathbf{F_{D,i}} + \mathbf{F_{R1,i}} + \mathbf{F_{R2,i}} = 0, \quad (1)$$

where $\mathbf{F_M}$ is the added mass force, $\mathbf{F_B}$ is the buoyancy force, and $\mathbf{F_D}$ is the drag force.

In this study we investigate the potential of DIH for assessing the bubble sizes, locations and the various forces appearing in Eq. (1) that act on moving acoustic bubbles. To do so, a step-by-step experimental methodology is proposed. In Section 2, the experimental setup and data analysis are presented. In Section 3, a single, free rising bubble is considered. It allows quantifying the added mass, buoyancy and drag force acting on it. In Section 4, a single bubble is driven in a standing wave field, and is trapped at a pressure antinode. The investigation of its translational motion results in the quantification of the primary radiation force. In Section 5, two bubbles coalescing at the same location are investigated, so that the secondary Bjerknes force can be predicted.

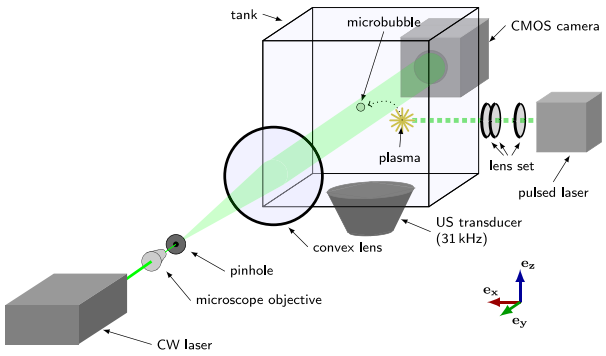

Fig. 1. Schematics of the experimental setup. A single vapor bubble is generated using a focused pulsed laser beam. After its collapse, the bubble is now constituted of non-condensable gases and moves in the acoustic field until it reaches the trapping zone. Simultaneously, the bubble trajectory is recorded by the in-line holographic system.

2. Experimental setup and optical techniques

2.1. Bubble nucleation, driving and trapping

A schematics of the experimental setup is given in Fig. 1. A 8-cm-edge cubic water tank is filled with filtered water. Single bubbles are nucleated inside the tank by focusing the second harmonic of a Nd:YAG pulsed laser (New Wave Research, Solo III, wavelength $\lambda_{YAG} = 532\,\text{nm}$ and $6\,\text{ns}$ pulse duration). The laser beam is focused by a set of three lenses: it is enlarged by a beam expander ($f = -25\,\text{mm}$); ($f = 125\,\text{mm}$) and finally focused by an aspherical lens ($f = 40\,\text{mm}$) to minimize optical aberrations. After their collapse, bubbles contain a small amount of non-condensable gas coming from the surrounding liquid due to diffusion and plasma recombination. At this stage, the typical size of air bubbles ranges from 30 to $80\,\mu\text{m}$.

A plane, Langevin-type ultrasound transducer (SinapTec®, diameter of the active area $35\,\text{mm}$) is attached to the bottom of the tank. Echographic gel is used to ensure (no air) impedance matching between the transducer and the tank. The transducer is driven by a sinusoidal wave field whose frequency is set to $31.25\,\text{kHz}$, corresponding to a resonant bubble radius $R_{res} \approx 104\,\mu\text{m}$ according to Minnaert's theory [36]. The voltage amplitude of the transducer is varied between 5 and $7.5\,\text{V}$, no gain amplifier is used. The driving frequency is set close to an acoustic mode of the cavity so that a standing wave field is established. As a consequence, once generated a bubble will move in the acoustic field until reaching a trapping zone. Because all the investigated bubbles are smaller than the resonant size, they are naturally driven towards the pressure antinodes due to the primary radiation force [16]. The different forces acting on the bubbles lead to a three-dimensional and non-intuitive trajectory. The characterization of the full bubble trajectory along its lifetime (from nucleation to its trapping location) requires the temporal measurement of the Cartesian coordinates $x(t)$, $y(t)$ and $z(t)$. The investigation of the forces that a bubble experiences also depends upon its radius R and the applied acoustic pressure. Tracking these different quantities by classical optical imaging is tricky as the trajectory of the investigated bubble can escape from the focal plane of the camera. In addition, the observation of small objects requires high image magnification, which leads to a significant decrease in the depth of field.

2.2. Digital in-line holography setup

To overcome these problems, we propose an original approach based on the use of digital in-line holography (DIH). DIH makes it possible to realize a Lagrangian tracking of small objects in a large

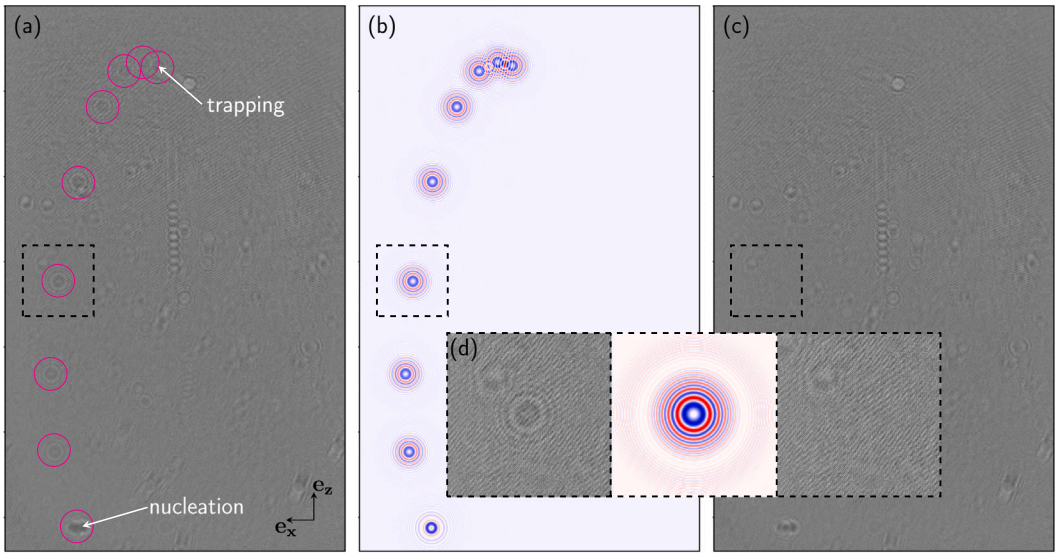

Fig. 2. A sequence of in-line holograms in the case of a bubble trapped in an acoustic field. A superimposition of nine holograms of the same bubble along its trajectory is shown: (a) the raw sequence including image background correction, (b) the best-matching synthetic holograms, (c) the residuals obtained by subtracting the synthetic holograms from the recorded holograms and (d) close-up of the recorded, synthetic and residual holograms for a given bubble location.

volume [29,31] together with an accurate measurement of their diameter. Bubbles are illuminated by a continuous wave laser beam (CNI MLL-FN, DPSS, $\lambda_{CW} = 532\,\text{nm}$, 400 mW). In order to "clean up" the laser beam, the later is focused by an objective microscope (20× magnification) onto a pinhole of ⌀10 µm in diameter. The laser beam is then collimated by a spherical convex lens ($f = 750\,\text{mm}$). A full-aperture obstruction target (obstruction diameter of ⌀492 µm) is used to determine the system magnification to 1.083. The holograms of the bubbles are recorded at a frequency of 400 fps on a 12-bit CMOS sensor (Vision Research V611) with a pixel size of 20 µm. This optical arrangement, shown in Fig. 1, allows us to probe an approximate liquid volume of $15 \times 25 \times 80\,\text{mm}^3$. This large volume includes both the nucleation and the trapping locations, and the motion of the bubble between them. The trajectories are recorded over a time interval of several seconds (up to 12 s) to ensure that the bubble has reached its trapping location and remained stable there.

2.3. Hologram processing

The reconstruction of holograms is performed with an inverse problem method [27] with an similar algorithm applied to the study of evaporating drops [30,37]. This approach is known to overcome the uncertainties and biases induced by the finite size of both the sensor and its pixels. In many applications, this method allows one to significantly increase the accuracy of the measurements. The inverse method reconstruction is based on the minimization of a cost function defined as the difference between the recorded hologram and a model hologram. The method was first introduced in Soulez et al. [27]. The method and algorithm used in this paper, including pixel integration and contrast adjustment, is detailed in Seifi et al. [29]. The hologram model describes the diffraction pattern of an opaque disk in the Fraunhofer approximation framework with summation of the incident beam [27]. Bubbles are first detected using a convolution process, from which a rough estimation of the 4 parameters x, y, z and diameter d is obtained. The minimization of the cost function is then performed by using a standard Levenberg–Marquardt algorithm.

In the present study, the bubbles are micrometric and are considered spherical, as demonstrated by the smallness of the Bond number Bo:

$$Bo = \frac{4\Delta\rho g R^2}{\sigma} \sim 10^{-4} \ll 1, \tag{2}$$

where $\Delta\rho$ is the difference in density between water and air, g is the gravitational acceleration, and σ is the surface tension between water and air. Also, the applied acoustic pressure is kept below the threshold for triggering nonspherical instability on the bubble surface [38], ensuring that the bubbles remain spherical during their motion. In addition to the large recording distance, a simple scalar diffraction model can be used for the description of the light diffracted by the bubbles, in the Fraunhofer approximation:

$$Fr = \frac{R^2}{L\lambda_{CW}} \sim 10^{-2} \ll 1, \tag{3}$$

where L is the distance between the water tank and the CMOS sensor. The diffraction of a bubble is therefore modeled by the diffraction pattern of an opaque two-dimensional disk relying on a set of four parameters: the coordinates (x, y, z) of their center and their radius R.

An example of image processing is shown in Fig. 2. Nine recorded holograms are shown along the trajectory of a bubble trapped in the acoustic field (Fig. 2(a)). The bubble holograms are hard to distinguish even after background correction and are encircled to ease their observation. The synthetic holograms that minimize the difference between the model and each recorded hologram are shown in Fig. 2(b). The difference between the synthetic and the recorded holograms is displayed on Fig. 2(c). These residuals are quite low (see Fig. 2(d)), illustrating the good determination of the position and bubble size. The only exception is the first hologram corresponding to the nucleation site. Indeed, the nucleation is the site of violent and highly nonlinear phenomena leading to an aspherical collapse, the fragmentation into several daughter bubbles or local variation of the refractive index due to thermal effects. Therefore, the diffraction model obviously fails to describe the recorded hologram in the first moments of the bubble lifetime.

3. Free rising bubble

As indicated in Eq. (1), the bubble trajectory in the acoustic levitator is governed by four forces: the buoyancy force $\mathbf{F_B}$, the drag force $\mathbf{F_D}$, the primary $\mathbf{F_{R1}}$ and the secondary $\mathbf{F_{R2}}$ radiation forces. In absence of the acoustic field, the last two forces can be removed from the equation of bubble translation. As a consequence, after laser nucleation, a bubble rises freely to the top of the tank due to buoyancy. The bubble moves

along a rectilinear trajectory, and its ascension velocity is conditioned by the drag force. The holographic measurements allows assessing the bubble location (hence its velocity) and size (hence the buoyancy force), so that the appropriate modeling of the drag force experienced by the bubble can be deduced. Holographic measurements performed on a free rising bubble are shown in Fig. 3. The bubble motion in two orthogonal plane are displayed in Figs. 3(a, b). The smallness of the associated standard deviation highlights is the good accuracy of the measurement. It has been estimated to $\sim 2\,\mu m$ on the transverse directions x and z (parallel to the sensor) and about $0.3\,mm$ (roughly three bubble diameters) on the depth direction y. The temporal evolution of the bubble radius during its ascension is shown in Fig. 3(c). The slow decrease of the radius suggests that the bubble slightly dissolves during its ascension. The prediction of the gas diffusion at the bubble interface is well represented by the Epstein–Plesset model:

$$\dot{R} = \left(C_\infty - C_{\text{surf}}\right) D_{\text{air}} \left(\frac{1}{R} + \frac{1}{\sqrt{\pi D_{\text{air}} t}} \right), \tag{4}$$

where the overdot denotes the time derivative, C_∞ and C_{surf} are the mass concentration in the saturated water and at the bubble interface, respectively, and $D_{\text{air}} = 2 \times 10^{-9}\,m^2\,s^{-1}$ is the diffusion coefficient of air. Considering a bubble with an initial radius of $49.5\,\mu m$, with a mass concentration at its interface equal to $C_{\text{surf}} = 2.4 \times 10^{-2}\,kg\,m^{-3}$ and located in a saturated water ($C_\infty = 8.3 \times 10^{-3}\,kg\,m^{-3}$), the evolution of its radius is shown in Fig. 3(c). A good agreement is obtained with the experimental evolution of the radius. The slight difference in the slope of the dissolution process may arise from the neglect of convective effects around the bubble in the Epstein–Plesset theory.

We can now infer the appropriate form for modeling the drag force. The knowledge of the bubble radius over time allows calculating the buoyancy force:

$$\mathbf{F_B} = \frac{4}{3}\left(\rho_\ell - \rho_g\right) \pi g R^3 \mathbf{e_z}, \tag{5}$$

where ρ_ℓ and ρ_g are the liquid and the bubble densities, respectively. The general formulation of the drag force can be written by:

$$\mathbf{F_D} = -\frac{1}{2}\rho_\ell \pi R C_D \, \|\mathbf{u}\| \cdot u_z \mathbf{e_z}, \tag{6}$$

where $\|\mathbf{u}\|$ is the magnitude of the bubble velocity (the liquid is supposed at rest), u_z is the velocity component along the $\mathbf{e_z}$ direction, and C_D is the drag coefficient. This coefficient is analytically undetermined in its general form [40–43]. However, it can be experimentally deduced under the assumption of null acceleration:

$$C_{D_{\text{DIH}}} = \frac{8}{3}\frac{\rho_\ell - \rho_g}{\rho_\ell}\frac{R^2 g}{\|\mathbf{u}\| \cdot u_z \mathbf{e_z}}. \tag{7}$$

The validity of the assumption of null acceleration during the bubble motion is confirmed by the quantification of the different forces acting on the bubble, as shown in Fig. 4(a).

Here, the inertia and buoyancy forces are calculated from the holographic measurements, while the drag force is deduced from the balance between the three involved forces. The buoyancy force decreases because of the bubble dissolution, and inertia remains negligible along the bubble trajectory. Fig. 4(b) shows the drag coefficient $C_{D_{\text{DIH}}}$ as a function of the Reynolds number in the log–log representation, for four different rising bubbles. It is worth noting that, because the bubble equilibrium radius decreases with time, its velocity decreases along the trajectory. As a consequence, Fig. 4(b) maybe read from the right to the left during the bubble ascension. The drag coefficient $C_{D_{\text{DIH}}}$ is compared to the cases of a bubble moving in a clean water (Hadamard and Rybczynski model [44]) or of a contaminated bubble (Oseen model [44]). Just after its nucleation, the bubble behaves like moving in a clean water. It becomes contaminated as it rises in the fluid and the associated drag coefficient tends to the Oseen relationship. Since there is no universal law for bubbles in a wide range of Reynolds number,

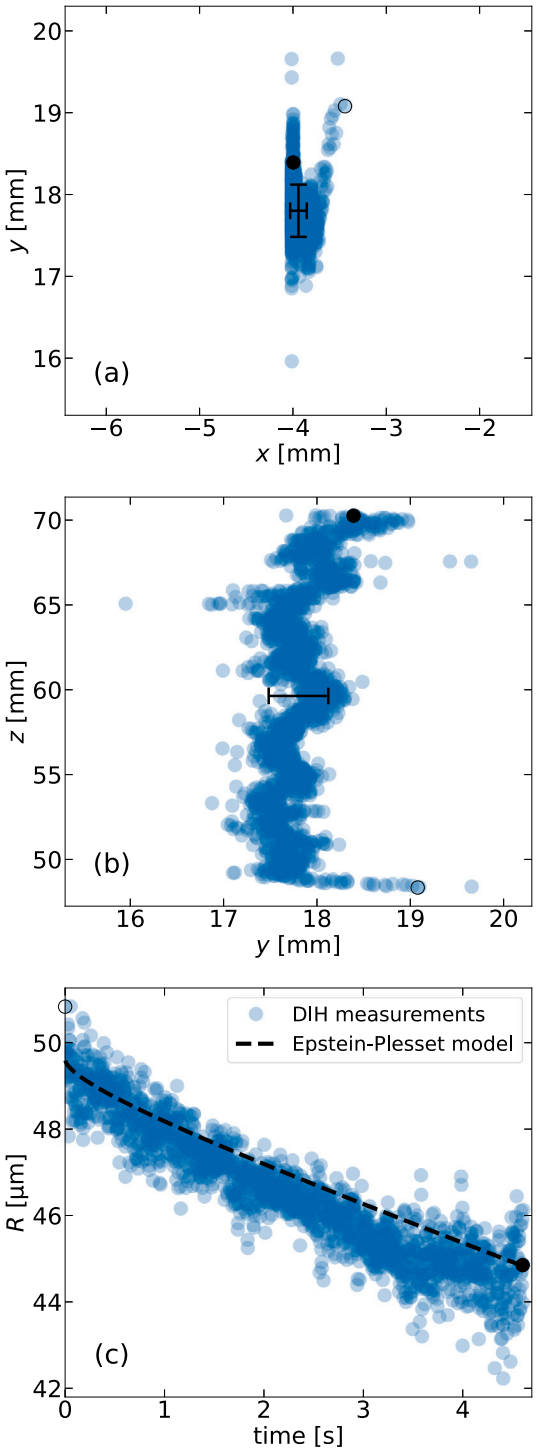

Fig. 3. DIH measurements using inverse problem approach (IPA) for a free rising bubble. Evolution of the bubble position in (a) the (x, y) plane and (b) the (y, z) plane, where the y axis refers to the optical axis. Black errorbars correspond to the standard deviation. (c) Evolution of the radius of the free rising bubble as a function of time. The dashed line corresponds to the Epstein–Plesset model [39] for bubble dissolution. The first (open circle) and last (filled circle) measured bubbles are shown for readability.

it is appropriate to consider the drag coefficient given by the standard drag curve (SDC), which is valid for bubbles in an untreated (tap) water for $Re < 10$ [40,41]. An approximation of the SDC has been proposed

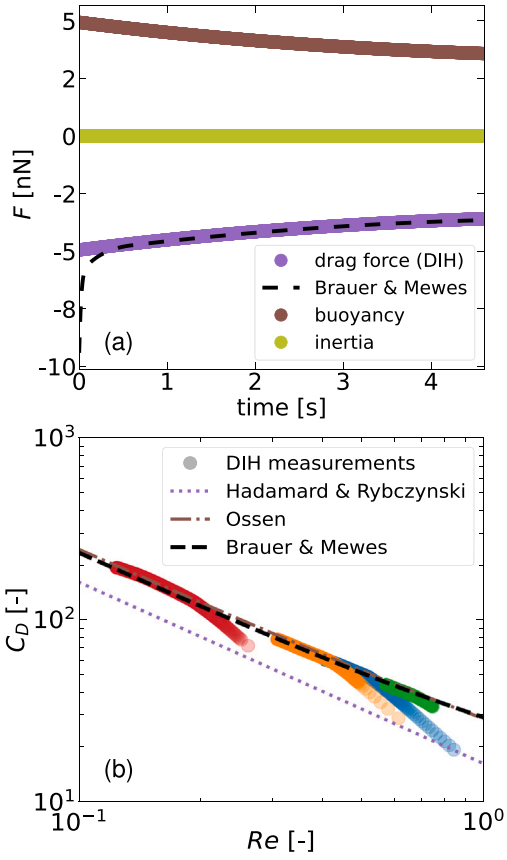

Fig. 4. (a) Temporal evolution of the forces acting on a rising bubble. The adjustment of the drag law with the Brauer and Mewes modeling is shown (dashed line). (b) Evolution of the drag coefficient $C_{D_{\text{DIH}}}$ as a function of the Reynolds number Re for four rising bubbles. The Hadamard and Rybczynski [44] (clean bubble) and the Oseen [44] (contaminated bubble) modeling are superimposed to the experimental data. The drag coefficient is also adjusted using the Brauer and Mewes [40] law once the bubble has reached its terminal velocity. Fitting parameters for the Brauer and Mewes model are $C_1 = 10$ and $C_2 = -5$.

by Brauer and Mewes [40]:

$$C_{D_{\text{SDC}}} = C_1 + \frac{C_2}{Re^{0.5}} + \frac{24}{Re}, \tag{8}$$

where C_1 and C_2 are fitting parameters. A good agreement of Eq. (8) with the experimental data is obtained for $C_1 = 10$ and $C_2 = -5$, as shown in the Figs. 4(a, b). We will therefore keep these values of the fitting parameters for the rest of the study.

4. A single bubble trapped in a stationary acoustic field

Now that the holographic measurements on a free rising bubble have shown their interest for the determination of the drag force, we consider the case of a single bubble submitted to an external acoustic field. After nucleating a single bubble when the acoustic field is activated, it moves until reaching a stable location. Fig. 5 shows the three components of the bubble location as a function of time measured by DIH. The motion of the bubble is obviously three-dimensional. The bubble coordinates were filtered using cubic spline interpolation in `SciPy` (open source Python library) to obtain smooth, regularized trajectories from noisy data. Velocity and acceleration were then derived analytically from the first and second derivatives of the splines, providing stable and accurate estimates of the bubble dynamics. In the

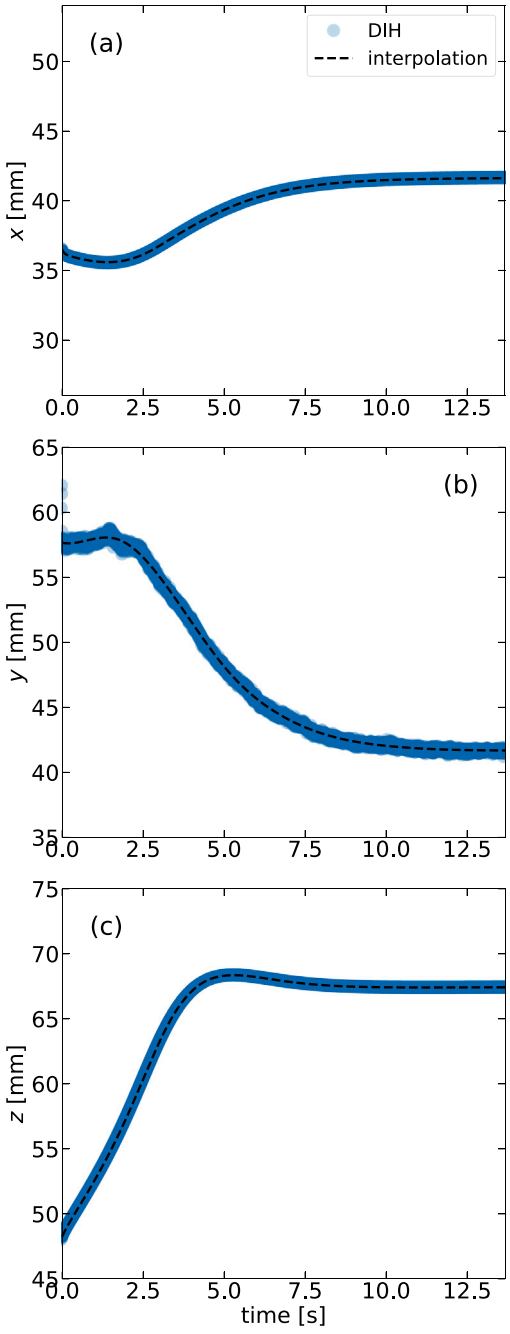

Fig. 5. DIH measurements using inverse problem approach (IPA) for a single bubble in the ultrasonic field. (a–c) Temporal evolution of the bubble position along the x, y and z direction, respectively.

(x, y) plane, the bubble reaches the center of the cavity (with identical x and y coordinates) after nearly eight seconds. Along the z direction, the bubble rises in the cavity until reaching a constant height (around $z = 67$ mm). Due to its entrainment, the bubble shortly exceeds the trapping altitude around $t = 5$ s. The experimental results clearly illustrate the trapping of the bubble at a particular location after $t = 10$ s.

The trapping of the bubble takes its origin from the primary radiation force $\mathbf{F_{R1}}$ induced by the ultrasound wave on the oscillating bubble:

$$\mathbf{F_{R1}} = -\langle V(t)\nabla p(\mathbf{r}, t)\rangle, \tag{9}$$

where $\langle\,\rangle$ denotes the time-averaging process over an acoustic period. The acoustic pressure field is

$$p(\mathbf{r},t) = p_{ac}\,p(x,y,z)\sin(\omega t), \tag{10}$$

where p_{ac} is the maximum acoustic pressure in the cavity, $p(x,y,z)$ is the dimensionless acoustic pressure at the coordinate (x,y,z), and ω is the angular frequency. Under moderate acoustic driving, the bubble undergoes linear oscillations, so that its radius writes $R(t) = R_0\left[1 - a_0\sin(\omega t)\right]$, with R_0 the time-averaged radius over an acoustic period, and $a_0 \ll R_0$. The radial expansion coefficient a_0 can be obtained by linearizing the Rayleigh-Plesset equation and retaining only the steady-state solution for undamped oscillations [1]:

$$a_0 = -\frac{p_{ac}\,p(x,y,z)}{\rho_\ell R_0\left(\omega_0^2 - \omega^2\right)}, \tag{11}$$

where ω_0 is the natural angular frequency of the bubble, first derived by Minnaert [36]. When surface tension and viscosity are taken into account in the Minnaert frequency, the natural angular frequency is given by

$$\omega_0^2 = \frac{1}{\rho_\ell R_0^2}\left[3\kappa\left(\frac{2\sigma}{R_0} + p_0 - p_v\right) - \frac{2\sigma}{R_0}\right], \tag{12}$$

where κ is the gas polytropic index, σ the liquid–gas surface tension, p_0 the atmospheric pressure and p_v is the vapor pressure. Replacing the linearized bubble volume $V(t) = V_0\left[1 - (3a_0/R_0)\sin(\omega t)\right]$ into Eq. (9) leads to the theoretical prediction of the primary radiation force

$$\mathbf{F}_{\mathbf{R1}}^{\mathrm{th}} = +\frac{2R_0p_{ac}^2}{\rho_\ell\left(\omega_0^2 - \omega^2\right)}p(x,y,z)\nabla p(x,y,z). \tag{13}$$

The analysis of Eq. (13) indicates that the primary radiation force is canceled when the pressure field or its gradient is null, meaning at the pressure nodes or antinodes. For bubbles smaller than the resonant size, or in other words, for bubbles driven below their resonance frequency $\omega < \omega_0$, the force is always directed towards a pressure antinode, whereas for bubbles larger than the resonant size (equivalently $\omega > \omega_0$), the force is always directed towards a pressure node. Also, dividing Eq. (13) by p_{ac}^2 allows us to free ourselves from the maximum acoustic pressure within the cavity, which remains unknown at this stage. We will see later how we can estimate this value from the holographic measurements.

In order to predict $\mathbf{F}_{\mathbf{R1}}^{\mathrm{th}}$ according to Eq. (13), one needs to know the spatial distribution of the dimensionless acoustic pressure $p(x,y,z)$ within the cavity. Since the cavity is closed, it is impossible to measure the acoustic pressure field without any perturbation of the field itself. We therefore propose to calculate the linear acoustic pressure field within the cavity using a multiphysics software (Comsol Multiphysics®).

The numerical simulations have been performed using Comsol Multiphysics 6.3, with the Geometry and Frequency domain module, assuming linear acoustic propagation. An optically transparent (PMMA) cubic tank (79 mm edge and 3 mm thickness per face) has been modeled in the Geometry module. The ultrasonic transducer is designed by a cylindrical surface (diameter 35 mm) centered at the bottom of the tank. The boundary conditions are set to zero pressure on each wall, and with a normal displacement amplitude of 1 μm at the transducer surface. Due to the cubic design of the tank, the simulation is three-dimensional. The mesh generation chosen is an unstructured tetrahedral volumetric mesh with an extremely fine size. The Frequency Response Function of the tank has been obtained using the Frequency domain module, and an acoustic resonance of the cavity is obtained at 31.25 kHz that correspond to the nominal frequency of the transducer. The simulated displacement amplitude of the transducer is unrealistic and leads to indicative pressure amplitudes. As a consequence, the dimensionless pressure field $p_{num}(x,y,z)$ is obtained by dividing the simulated pressure amplitude by the maximum pressure in the cavity. Fig. 6(a) presents the isocontours of pressure in the tank. The sectional views (Figs. 6(b, c)) show the spatial distribution of the pressure field in two orthogonal planes. The antinode with the highest amplitude (white star in Figs. 6(b–c)) is located above the transducer (at the center of the tank) and at roughly two thirds of the height. The superimposition of the bubble trajectory and the numerical dimensionless pressure field in the cavity is presented in Fig. 7(a).

As expected, the bubble is trapped slightly above the pressure maximum due to the balance with the buoyancy force. Along the bubble trajectory, the profile of the dimensionless acoustic pressure is extracted and displayed in Fig. 7(b). It is worth noting that the bubble is supposed to cross a pressure node in the first moments following the nucleation. The evolution of the bubble radius as a function of time is shown in Fig. 7(c). Similarly to the case of a free rising bubble, the mean bubble radius decreases with time due to the dissolution process. The relatively small variations of the bubble radii around its equilibrium value indicates that linear radial bubble oscillations can be assumed. The expansion coefficient a_0 of the bubble oscillations is therefore estimated by replacing the numerical prediction of the acoustic pressure along the path of the bubble (Fig. 7(b)) in Eq. (11). In fact, it is more appropriate to replace the numerator of Eq. (11) by $\alpha p_{ac}p_{fit}(x,y,z)$, where $p_{fit}(x,y,z)$ is the numerical acoustic pressure shown in Fig. 7(b) and approximated by a polynomial expansion, and $\alpha = 0.257$ is a adjustment factor ensuring an identical baseline dispersion between the data with (Fig. 7(b)) and without (Fig. 3(c)) activation of the acoustic field. The value of α is chosen in order to fit the predicted primary radiation force at the end of the trajectory. We will see in Section 5 that this value is also relevant for the estimation of the secondary radiation force. The only fitting parameter is the maximal acoustic pressure p_{ac} that is estimated to be 7.3 kPa. The predicted radial oscillations are superimposed on the measured bubble radii in Fig. 7(c). A relatively good agreement is obtained between the measured bubble radii and the predicted ones.

The primary radiation force $\mathbf{F}_{\mathbf{R1}}^{\mathrm{DIH}}$ obtained by DIH can now be quantified. To do so, the components of the bubble velocity and the acceleration are calculated from the interpolated components of the bubble displacement (Figs. 5(a–c)), in order to remove high-frequency noise. The inertia, buoyancy and drag forces are obtained in a similar way to the one discussed in Section 3. The remaining unknown in Eq. (1) is therefore the primary radiation force. Figs. 8(a–c) shows the x, y and z components of the four involved forces, and the magnitude of the primary radiation force $\mathbf{F}_{\mathbf{R1}}^{\mathrm{DIH}}$ is presented in Fig. 8(d). From the nucleation site ($t = 0$ s) towards the trapping location ($t > 12.5$ s), the bubble is not experiencing a significant acceleration, so that the inertia term can be disregarded from the force balance equation. Along the x and y direction, the components of the primary radiation force and of the drag force are hence of the same amplitude but with opposite sign, because the buoyancy plays no role in the (x, y) plane. At $t \sim 1.5$ s, both the x and y components are null, suggesting that the bubble has crossed a pressure node. This is confirmed by the simultaneous cancellation of the z component of $\mathbf{F}_{\mathbf{R1}}^{\mathrm{DIH}}$ (Fig. 8(c)). The vertical component of $\mathbf{F}_{\mathbf{R1}}^{\mathrm{DIH}}$ slightly differs from the balance with the drag force due to the buoyancy term. When reaching the trapping zone, the primary radiation force is exactly opposite to the buoyancy force with a magnitude of $\mathbf{F}_{\mathbf{R1}}^{\mathrm{DIH}} \sim 3$ nN. The cancellation of the x and y components of the radiation force for $t > 10$ s indicates that the bubble is trapped exactly at the vertical of the theoretical trapping location. The numerical prediction of the primary radiation force is also shown in Fig. 8. The numerical prediction is deduced by replacing the numerical pressure field and its gradient in Eq. (13), and by considering the maximal acoustic pressure p_{ac} to be 7.3 kPa. A good agreement is obtained between the trend of the numerical and experimental radiation forces, with a slight temporal shift. Particularly, similar magnitudes of the order of a few nN are obtained.

The amplitudes of the y and z components of the involved forces are shown in Fig. 9 along the bubble trajectory and superimposed on

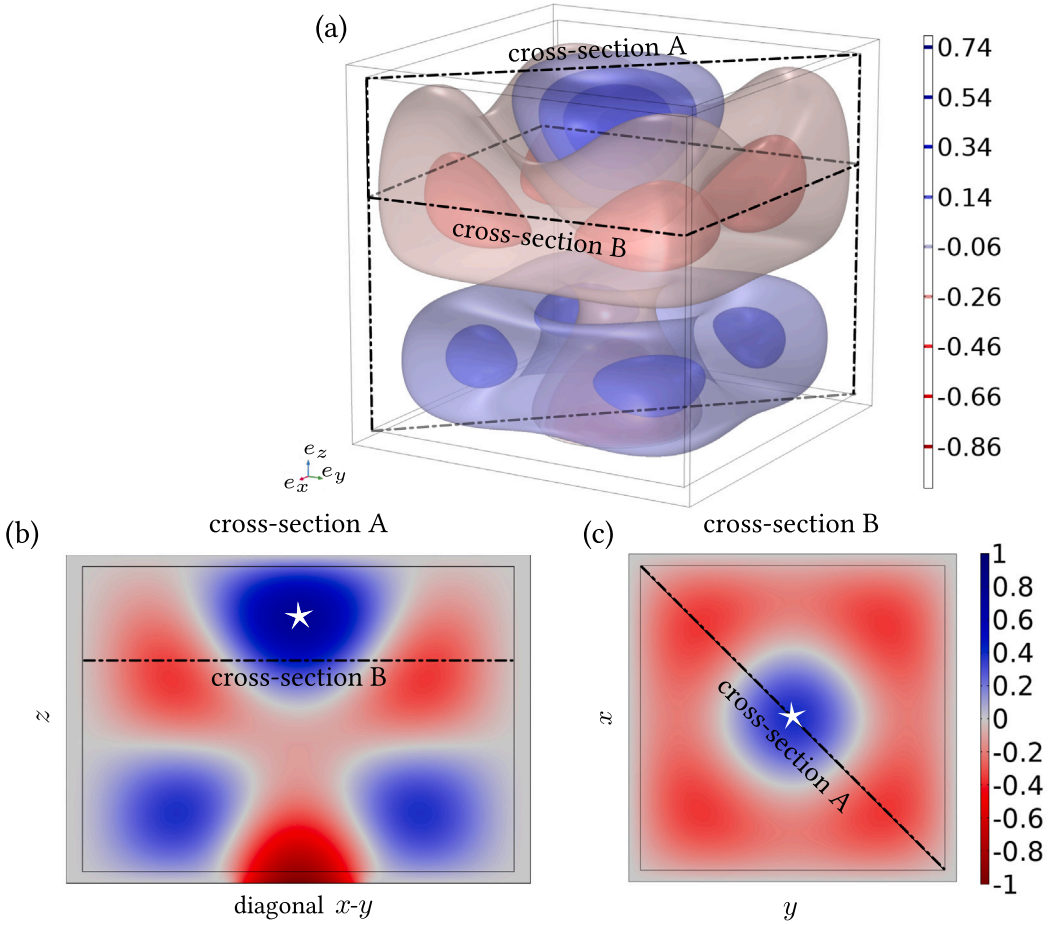

Fig. 6. Distribution of the dimensionless acoustic pressure within the acoustic chamber. (a) Three-dimensional representation for different isocontours of the pressure field at the driving acoustic frequency. (b) Distribution of the acoustic pressure in the diagonal plane of the cavity. (c) Distribution of the acoustic pressure in a horizontal (at a constant height z) plane. The height has been chosen such that it corresponds to the location of the pressure antinode in the upper part of the cavity. The white star indicates the location of the antinode with the highest amplitude.

the numerical pressure field. Five instants between the nucleation and the trapping are displayed. The corresponding pressure and pressure gradient along the z direction are shown in Fig. 9(f). The positioning of the nucleation site (location (a)) near a pressure node is clearly visible and results in a negligible primary radiation force. Then the bubble rises only vertically (location (b)) until the y component of the radiation force becomes large enough to deviate the bubble trajectory (location (c)) towards the pressure antinode. Midway, between locations (b) and (c), the z component of the radiation forces is canceled as the vertical pressure gradient cancels (Fig. 9(f)). Then the bubble slowly reaches the trapping site: the magnitude of the drag force decreases significantly (location (d)) and the remaining forces are the buoyancy force and the vertical component of the radiation force (location (e)).

5. The case of two colliding bubbles

The designed levitation chamber allows one to observe the coalescence between a bubble trapped near a pressure antinode and another incoming bubble. This technique has been used to trigger axisymmetric nonspherical oscillations in a controlled way in a sufficiently strong acoustic field [45]. Here the same methodology is performed in order to assess the secondary radiation force by DIH. To do so, the following procedure is conducted: a single, micrometric bubble is nucleated at a few millimeters from a pressure antinode of the acoustic field. The bubble is then driven towards, and trapped at, the pressure antinode as discussed in Section 4. A second bubble is nucleated, and its trajectory is influenced both by the primary radiation force and the secondary radiation force acting between the two bubbles. Due to the primary Bjerknes force, the second bubble will reach the same pressure antinode where the first bubble has been trapped. The two bubbles will then mutually attract as they are both smaller than the resonant size [46], and coalesce. Figs. 10(a–c) shows the three components of the displacement of the incoming, already-trapped and coalesced bubbles. The temporal evolution of the radii of the three bubbles is shown in Fig. 10(d). Since no influence of the trapped bubble on the incoming one is expected at large distances, only the last two seconds of the trajectory are displayed. At the exception of the last moment of the recording when the encounter of the two bubbles occurs, the components of the displacements of both bubbles are smooth functions of time. The trapped bubble remains at the trapping location until the very last moments preceding the coalescence. During the first 7.5 s, the incoming bubble approaches the trapped site as if the trapped bubble were absent. It means that the incoming bubble is subjected only to the primary radiation force on that duration. During the last 0.5 s of the recording, the two bubbles deviate from their quasi-rectilinear trajectory. Their velocities increase significantly just before they encounter. The results demonstrate that the DIH technique allows us to probe the encounter of the two bubbles with a high temporal resolution.

It can be noticed in Fig. 10(d) that the bubble radii do not evolve much with time in the time interval. Indeed, the dissolution process is predominant during the first 5 s of the bubble motion, as observed in Fig. 7(c) in the case of a single trapped bubble. The equilibrium

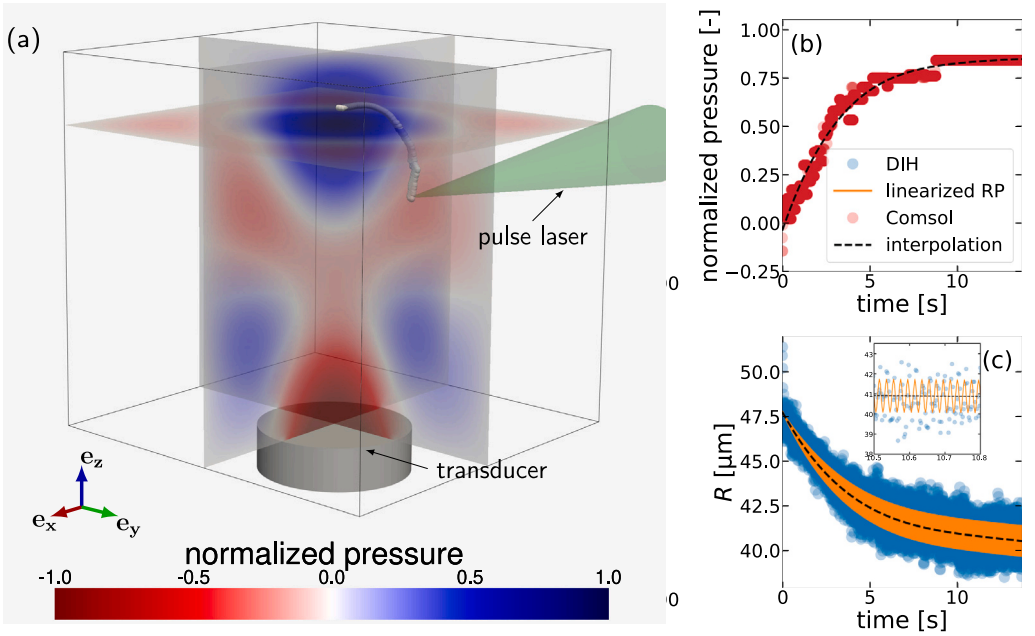

Fig. 7. DIH measurements using inverse problem approach (IPA) for a single bubble in the ultrasonic field. (a) Superimposition of the measured bubble trajectory and the numerical acoustic field. (b) Temporal evolution of the dimensionless pressure experienced by the oscillating bubble along its trajectory. (c) Temporal evolution of the bubble radius. The prediction of the linearized Rayleigh-Plesset equation is superimposed. The insert shows the numerical and experimental bubble oscillations on a dozen of acoustic periods. For all the graphs, blue circles indicate the DIH measurements, the dashed line refers to the interpolated data, the solid line to the solution of the linearized Rayleigh-Plesset equation, and the red circles to the numerical prediction from Comsol Multiphysics®.

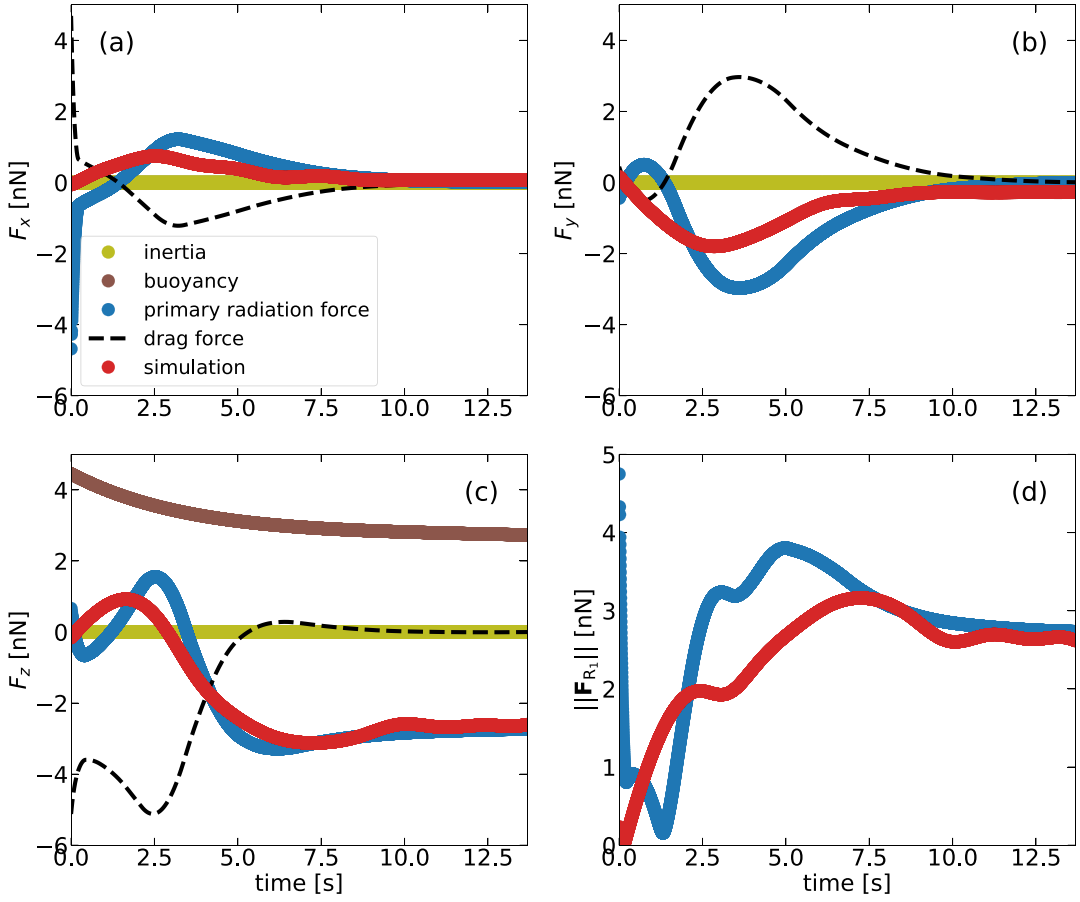

Fig. 8. Temporal evolution of the forces acting on a bubble moving in a standing wave field. The three components of each force are displayed (a–c) as well as the magnitude of the primary radiation force (d). The numerical prediction of the primary radiation force is provided for comparison.

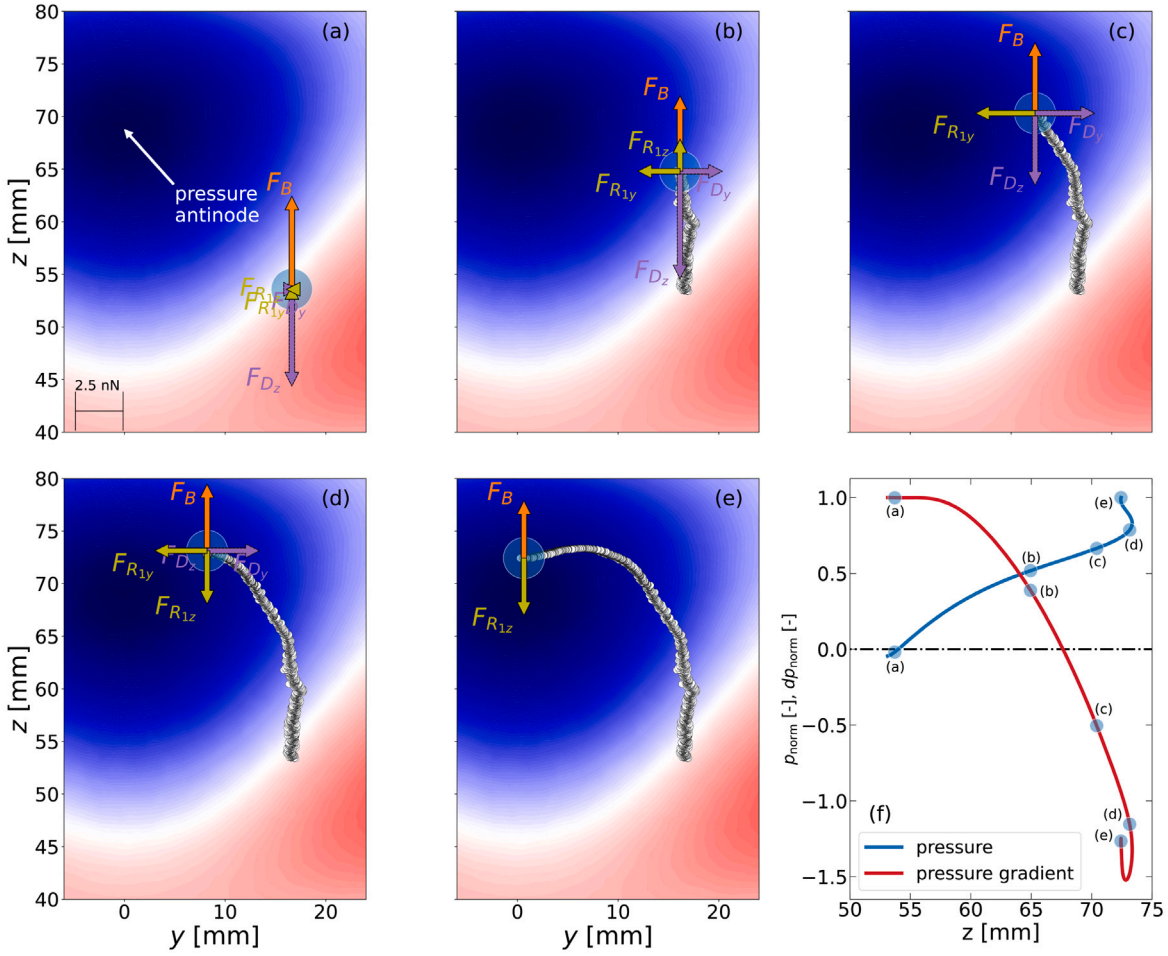

Fig. 9. (a–e) Superimposition of the y and z components of the involved forces and of the numerical pressure field. Five times are displayed along the bubble trajectory. (f) Evolution of the amplitudes of the acoustic pressure and of the vertical component of the pressure gradient.

radii of the incoming and already trapped bubbles are $R_{01} \sim 45\,\mu m$ and $R_{02} \sim 47\,\mu m$, respectively. The resulting coalesced bubble should have an equilibrium radius $R_{03} \sim 58\,\mu m$ using the conservation of volume. The DIH measurement of the radius of the coalesced bubble around $t = 7.7\,s$ predicts a singular value of $70\,\mu m$ followed by a stable equilibrium radius around $58\,\mu m$. The singular value is attributed to the nonsphericity of the bubble at the moment of coalescence. One frame later, the equilibrium radius measured by DIH reaches the expected radius for the coalesced bubble. It is worth noticing that the appearance of the singular radius can be used as a signature of the exact occurrence of coalescence.

In a similar way to the method proposed in Section 4, the amplitude of the acoustic radiation forces can be deduced from the DIH measurement. The components of the bubble velocity and the acceleration are calculated from the interpolated components of the bubble displacement (Figs. 10(a–c)). The inertia, buoyancy and drag forces are obtained as in Section 3. The remaining unknowns in Eq. (1) are therefore the sum of the two radiation forces $\mathbf{F_{R1,i}}+\mathbf{F_{R2,i}}$, shown in Fig. 11(a).

In order to separate the contribution of the each force in this summation, we assume that the long-range influence of the secondary radiation force is negligible in comparison to the primary radiation force, and that the attracting force only acts when the two bubbles are sufficiently close. This hypothesis is confirmed by analyzing the amplitude of the measured radiation forces in Fig. 11(a). Indeed, the amplitude of the term $\mathbf{F_{R1,i}} + \mathbf{F_{R2,i}}$ remains constant over a wide temporal range, until the very last moment preceding the coalescence. Near the trapping location, the primary radiation force is supposed to be constant in a small spatial area. The primary radiation force is therefore extrapolated by a linear fit (dashed line in Fig. 11(a)), and the secondary radiation force is deduced by removing the fitted component $\mathbf{F_{R1,i}}$ from the measured forces. The amplitude of $\mathbf{F_{R2,i}}$ is 0 far from the coalescence moment and increases to 70 nN at the last frame preceding the coalescence. The secondary Bjerknes force $\mathbf{F_{R2,i}}$ can be deduced from Eq. (1) applied to each bubble along the whole trajectory. A close-up on this attractive force is given in Fig. 11(b), not as a function of time but as a function of the inverse of the squared interbubble distance $1/d^2$. When the two bubbles are far from each other, the secondary radiation force has a negligible amplitude around 20 pN that corresponds to the measurement noise. For the interbubble distance $d \sim 1.8\,mm$ (corresponding to $1/d^2 \sim 0.3$), the amplitude of the secondary radiation force suddenly increases and tends to a linear relationship with $1/d^2$. This behavior is expected from the theoretical modeling of the secondary radiation force first developed by Bjerknes [33] in the form:

$$\mathbf{F_{R2,i}} = 2\pi\rho|C|^2 G_B \mathbf{u}, \tag{14}$$

where C is the complex amplitude of the liquid velocity potential, $\mathbf{u}$ is the unit vector directed from the center of the ith bubble to the one of the jth bubble, and the coefficient G_B (B stands for Bjerknes) is a function of the mechanical properties of the system (bubble equilibrium radii, damping coefficient), the driving angular frequency and the

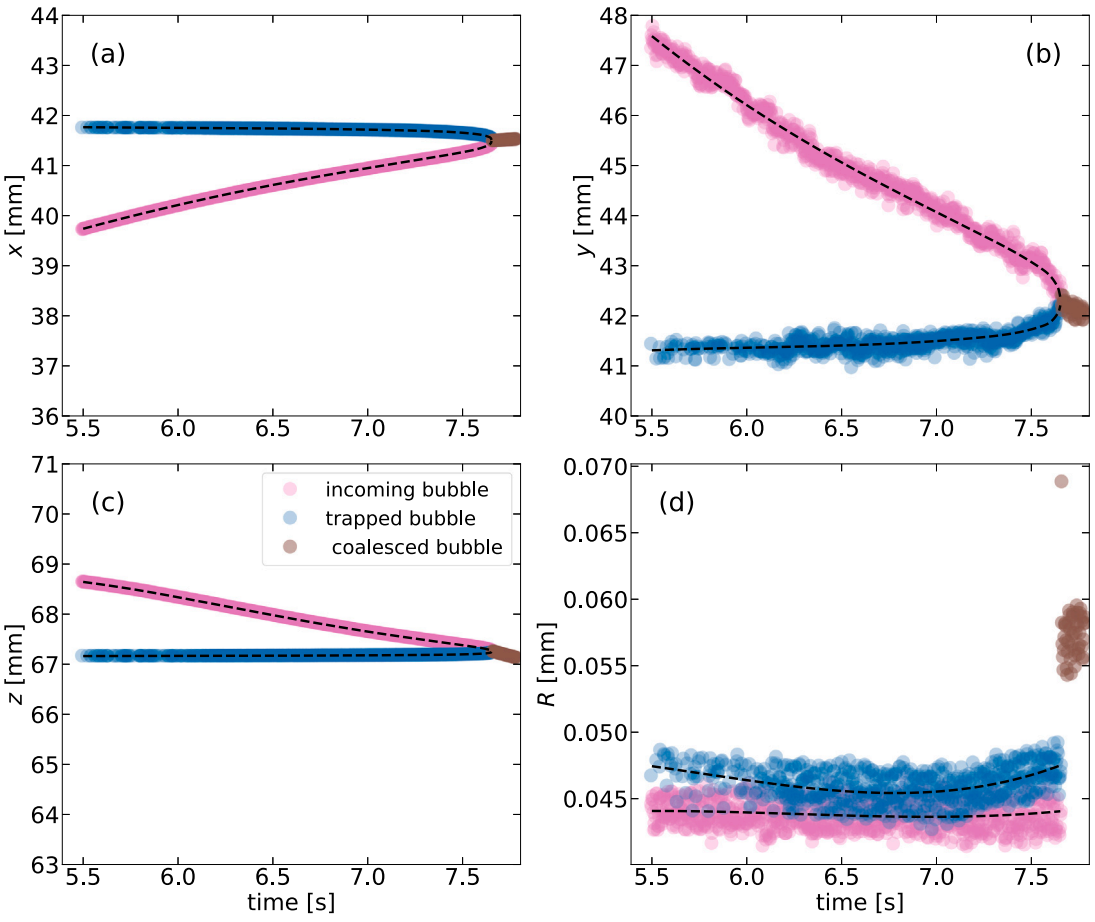

Fig. 10. DIH measurements using inverse problem approach (IPA) for the case of two coalescing bubbles. (a–c) Temporal evolutions of the bubble position along the x, y and z direction, respectively. (d) Temporal evolution of the bubble radii. Only the last two seconds of the trajectories are shown.

interbubble distance. This parameter is given by:

$$G_B = \frac{R_{01}R_{02}}{d^2}\frac{(1-\omega_1^2/\omega^2)(1-\omega_2^2/\omega^2)+\delta_1\delta_2}{\left[(1-\omega_1^2/\omega^2)^2+\delta_1^2\right]\left[(1-\omega_2^2/\omega^2)^2+\delta_2^2\right]}, \tag{15}$$

where $\delta_j = 3\gamma p_{j0} d_j/(\rho\omega^2 R_{0j}^2)$ is the damping coefficient for bubble j with $j = 1, 2$ and $p_{j0} = p_0 + 2\sigma/R_{0j}$. The coefficient d_j is calculated by using the following equations:

$$\frac{d_j}{b_j} = 3(\gamma-1)* \frac{X\sinh(X)+\sin(X)-2(\cosh(X)-\cos(X))}{X^2(\cosh(X)-\cos(X))+3(\gamma-1)X(\sinh(X)-\sin(X))}, \tag{16}$$

$$b_j = \left[\left(1+\frac{d_j^2}{b_j^2}\right)\left(1+\frac{3(\gamma-1)(\sinh(X)-\sin(X))}{X(\cosh(X)-\cos(X))}\right)\right]^{-1}, \tag{17}$$

$$X = R_{0j}(2\omega\rho_{gj}c_{pg}/k_g)^{1/2}, \tag{18}$$

where γ is the specific heat ratio, $\rho_{gj} = \rho_{gA}p_{j0}/p_A$ is the equilibrium density of the gas inside bubble j, ρ_{gA} is the gas density at the atmospheric pressure p_A, c_{pg} is the specific heat of the gas at constant pressure, and k_g is the thermal conductivity of the gas. Eq. (15) is valid when the spacing between the bubbles is much larger than their radii, or equivalently, when $d/(R_{01}+R_{02}) \gg 1$. In order to impose no restriction on the separation distance between the bubbles, Doinikov and Zavtrak [47] have developed a modeling in which the interaction force is expressed in terms of an infinite sum of powers of the small parameter R_{01}/d. We have checked that, in the case of bubbles smaller than the resonant size, accounting for multiple scattering between bubbles does not modify the behavior of the secondary radiation forces for all the investigated interbubble distances. Indeed, when the two bubbles are larger than the resonant size, accounting for multiple scattering leads to a change in the sign of the secondary radiation force. Due to the sign reversal of the interaction force, the motion of the two bubbles can change from attraction to repulsion. The sign reversal of the interaction force occurs at short separation distances between the two bubbles, and is at the origin of a new dynamically-stable equilibrium between the two bubbles which, instead of coalescing, stay close to each other at a distance less than a bubble radius [48]. In the present study, bubbles smaller than the resonant size are considered. In such as case, the behavior of the secondary radiation force with the interbubble distance shows no significant modification when accounting for multiple scattering or not. Due to the complexity of the mathematical form of the interaction force accounting for multiple scattering effects, the bubble-bubble interactions have been disregarded when discussing the form of the coefficient G_B appearing in the Eq. (14), given in a simplified form by Eq. (15). The secondary radiation force given by Eq. (14) is shown in Fig. 11(b). The extrapolated secondary radiation forces follows the $1/d^2$ dependency predicted by the modeling for interbubble distance smaller than $d \sim 1$ mm. The amplitudes of the measured attraction forces by DIH are in excellent agreement with the theoretical modeling, even when the two bubbles are close to the coalescence moment.

6. Discussion

The motion of micrometric bubbles in a field of view of several cubic centimeters is captured using an original digital in-line holography setup adapted to the visualization of small objects in a large region of interest (ROI). Indeed, the investigated bubble diameters are a

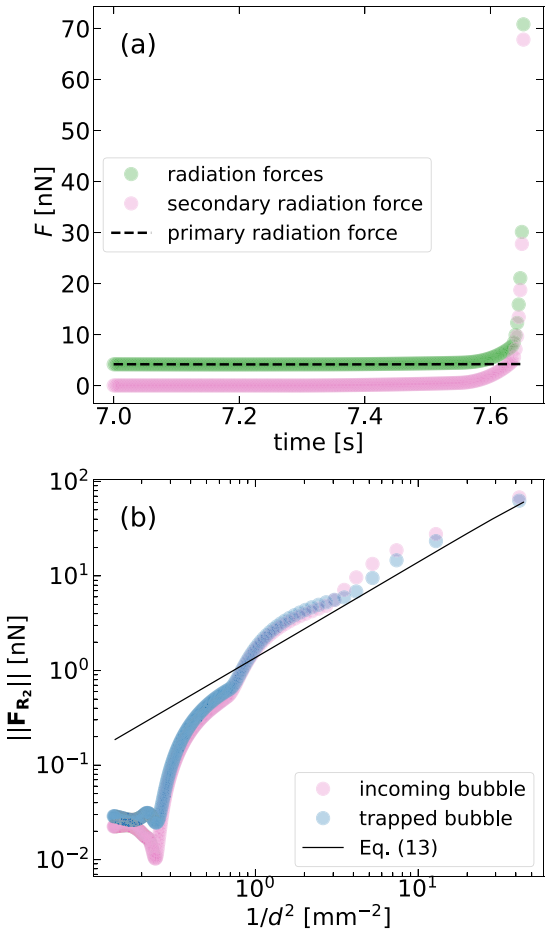

Fig. 11. Estimation of the acoustic radiation forces using the DIH measurements. (a) The secondary radiation force is deduced by removing the fitted component of the primary radiation force from the measured forces. (b) The extracted secondary radiation forces on the incoming and trapped bubbles are plotted in a logarithmic scale as a function of $1/d^2$, where d is the interbubble distance. A theoretical modeling accounting for multiple scattering is superimposed.

hundred micrometers, while the probed volume is $15 \times 25 \times 80\,\mathrm{mm}^3$, with one order of magnitude between each space dimension of the ROI in comparison to the bubble size. The limit size of the ROI is ruled by the size of the camera sensor, and can be adjusted using appropriate optical lenses. After nucleation in a medium at rest (no ultrasound), the bubble rises towards the upper surface due to buoyancy force. The large field of view allows capturing the bubble rise during several seconds. The dissolution process acting on the bubble volume is recovered using the Epstein–Plesset diffusion law (Fig. 3(c)). In parallel, the analysis of the bubble rising velocity allows determining the appropriate modeling of the drag force acting on it. The Brauer and Mewes approximation of the standard drag curve is found to coincide with the experimental drag force over a wide range of Reynolds number (Fig. 4).

While the rising motion of a free bubble is rectilinear, switching the ultrasound on implies the appearance of a radiation force acting on the bubble. Due to the three-dimensional characteristics of the acoustic field within the cavity (Fig. 6), the primary radiation force acting on the bubble acts along the three space dimensions and generates a complex 3D motion of the bubble (Fig. 5). Capturing the bubble motion during a dozen of seconds along three dimensions of space is out of the capability of common imaging techniques, where the bubble trajectory has to belong to the camera focal plane. Due to this limitation many studies have investigated the ultrasound-induced trapping of bubbles only in the last moment of the trajectory [35,45,49] and therefore only focus on the final quasi-rectilinear motion of the bubble approaching its trapping location. The scanning of the bubble trajectory within the cavity on a long path allows calculating the radiation force (Fig. 8), and hence the acoustic pressure and its gradient (Fig. 9) along the bubble trajectory. This methodology can be repeated with several bubbles nucleated at randomized locations in the cavity in order to map indirectly the acoustic pressure field, without using any hydrophone or other invasive probe. When a second bubble is nucleated while the first one has been already trapped, coalescence occurs and can be captured by DIH far before the coalescence moment, during and after the two bubbles have merged. It is shown that the exact moment of coalescence can be extracted from a singular value of the predicted bubble radius, which probably originates from the temporarily nonspherical shape of the bubble at the moment of merging. By analyzing separately the bubble trajectory far from the trapping location (where the primary radiation force is dominant over the secondary one) from the final moments preceding coalescence, the primary and secondary radiation forces acting on each bubble are deduced (Fig. 11). The estimated secondary radiation force is found to be in excellent agreement with the Bjerknes modeling of interacting forces between bubbles. Both the quadratic dependence of the force with the interbubble distance, and its absolute value of the order of some nN, are recovered.

To the best of our knowledge, this is the first time that a unique experimental setup allows quantifying the various phenomena investigated here: the dissolution process, the viscous drag, the ultrasound-induced and the bubble-induced radiation acting on a bubble. Usually specific setups are designed for investigating these different effects, particularly when one wants to quantify the interaction force acting between two acoustic bubbles [49,50]. The DIH setup possesses the advantages of being non invasive, simple to set, and providing an excellent resolution in the (x, z) camera plane. The resolution is slightly degraded in the third (optical) dimension but can be significantly improved using an inverse approach for the hologram detection. It is worth noting that several limitations need further investigations for improving the applicability of the DIH techniques for real-time monitoring of bubble clouds. Firstly, the analysis of a thousand holograms (corresponding to a single bubble trajectory tracked with a high-frame rate camera during several seconds) requires a full day when using 32 computing cores. The development of new reconstruction algorithms and the use of parallelized computer facilities can significantly reduce the duration of the post-analysis. Secondly, the hologram reconstruction is here adapted to spherical bodies only. With the aim of extending these techniques to nonspherical bubbles, new algorithms are required with an expected longer calculation time. Finally, dense bubble ensembles can theoretically be investigated since superimposed holograms can be distinguished using an inverse approach. However, due to the weak signal-to-noise ratio of the bubble hologram and the complex physics underlying acoustic bubble clouds, such an analysis is yet far from our experimental capabilities, and remains challenging.

7. Conclusion

A digital in-line holography technique (DIH) is proposed to capture non-invasively the three-dimensional motion of micrometric bubbles in an acoustic field. Both the dissolution process, viscous drag force, primary and secondary radiation forces acting on a single bubble or on two merging bubbles are quantified. All these forces are in excellent agreement with the theoretical predictions of each of these phenomena. The DIH technique thus appears as a simple, non invasive technique for investigating bubble phenomena in complex acoustic environments, where three-dimensional motion, bubble fragmentation or merging may occur.

CRediT authorship contribution statement

Cyril Mauger: Writing – review & editing, Writing – original draft, Visualization, Validation, Methodology, Investigation, Formal analysis, Data curation, Conceptualization. **Claude Inserra:** Writing – review & editing, Writing – original draft, Visualization, Validation, Methodology, Formal analysis, Conceptualization. **Antoine Lotton:** Writing – review & editing, Resources. **Nathalie Grosjean:** Writing – review & editing, Resources. **Alexander A. Doinikov:** Writing – review & editing. **Philippe Blanc-Benon:** Writing – review & editing. **Loïc Méès:** Writing – review & editing, Validation, Software.

Declaration of competing interest

The authors declare that they have no known competing financial interests or personal relationships that could have appeared to influence the work reported in this paper.

Acknowledgments

This project was funded by l'Agence Nationale de la Recherche (ANR), France, Project No. ANR-22-CE92-0062 and Project No. ANR-23-CE51-0023, and was supported by the LabEx CeLyA of the University of Lyon (No. ANR-10-LABX-0060/ANR-11-IDEX-0007).

References

[1] T. Leighton, The Acoustic Bubble, Academic Press, 1994.
[2] F. Reuter, S. Lauterborn, R. Mettin, W. Lauterborn, Membrane cleaning with ultrasonically driven bubbles, Ultrason. Sonochemistry 37 (2017) 542–560.
[3] T.J. Mason, Sonochemistry, vol. 2, Oxford University Press, New York, 1999.
[4] K.B. Bader, G. Bouchoux, C.K. Holland, Sonothrombolysis, in: J.-M. Escoffre, A. Bouakaz (Eds.), Therapeutic Ultrasound, Springer International Publishing, 2016, pp. 339–362.
[5] C.C. Coussios, R.A. Roy, Applications of acoustics and cavitation to noninvasive therapy and drug delivery, Annu. Rev. Fluid Mech. 40 (2008) 395–420.
[6] K. Hynynen, N. McDannold, N.A. Sheikov, F.A. Jolesz, N. Vykhodtseva, Local and reversible blood–brain barrier disruption by noninvasive focused ultrasound at frequencies suitable for trans-skull sonications, NeuroImage 24 (1) (2005) 12–20.
[7] K.-T. Chen, W.-Y. Chai, Y.-J. Lin, C.-J. Lin, P.-Y. Chen, H.-C. Tsai, C.-Y. Huang, J.S. Kuo, H.-L. Liu, K.-C. Wei, Neuronavigation-guided focused ultrasound for transcranial blood-brain barrier opening and immunostimulation in brain tumors, Sci. Adv. 7 (6) (2021).
[8] P.R. Birkin, D.G. Offin, T.G. Leighton, An activated fluid stream – New techniques for cold water cleaning, Ultrason. Sonochemistry 29 (2016) 612–618.
[9] W. Lauterborn, T. Kurz, Physics of bubble oscillations, Rep. Progr. Phys. 73 (10) (2010) 106501.
[10] U. Parlitz, R. Mettin, S. Luther, I. Akhatov, M. Voss, W. Lauterborn, Spatio–temporal dynamics of acoustic cavitation bubble clouds, Philos. Trans. R. Soc. Lond. Ser. A Math. Phys. Eng. Sci. 357 (1751) (1999) 313–334.
[11] P.C. Duineveld, The influence of an applied sound field on bubble coalescence, J. Acoust. Soc. Am. 99 (1) (1996) 622–624.
[12] M. Postema, P. Marmottant, C.T. Lancée, S. Hilgenfeldt, N. de Jong, Ultrasound-induced microbubble coalescence, Ultrasound Med. Biol. 30 (10) (2004) 1337–1344.
[13] M.S. Longuet-Higgins, The crushing of air cavities in liquid, Philos. Trans. R. Soc. Lond. Ser. A Math. Phys. Eng. Sci. 439 (1907) (1992) 611–626.
[14] T. Yamamoto, S.-I. Hatanaka, S.V. Komarov, Fragmentation of cavitation bubble in ultrasound field under small pressure amplitude, Ultrason. Sonochemistry 58 (2019) 104684.
[15] A. Eller, H.G. Flynn, Rectified diffusion during nonlinear pulsations of cavitation bubbles, J. Acoust. Soc. Am. 37 (3) 493–503.
[16] L.A. Crum, Measurements of the growth of air bubbles by rectified diffusion, J. Acoust. Soc. Am. 68 (1) (1980) 203–211.
[17] F. Burdin, N.A. Tsochatzidis, P. Guiraud, A.M. Wilhelm, H. Delmas, Characterisation of the acoustic cavitation cloud by two laser techniques, Ultrason. Sonochemistry 6 (1) (1999) 43–51.
[18] S. Labouret, J. Frohly, Study in a UHF electromagnetic resonant cavity of a bubble field induced by ultrasonic cavitation, Eur. Phys. J. AP 10 (3) (2000) 231–237.
[19] S. Labouret, J. Frohly, Bubble size distribution estimation via void rate dissipation in gas saturated liquid. Application to ultrasonic cavitation bubble fields, Eur. Phys. J. AP 19 (1) (2002) 39–54.
[20] R. Pflieger, G. Audiger, S.I. Nikitenko, M. Ashokkumar, Impact of bubble coalescence in the determination of bubble sizes using a pulsed US technique: Part 2 – effect of the nature of saturating gas, Ultrason. Sonochemistry 73 (2021) 105537.
[21] J. Lee, M. Ashokkumar, S. Kentish, F. Grieser, Determination of the size distribution of sonoluminescence bubbles in a pulsed acoustic field, J. Am. Chem. Soc. 127 (48) (2005) 16810–16811.
[22] A. Brotchie, F. Grieser, M. Ashokkumar, Effect of power and frequency on bubble-size distributions in acoustic cavitation, Phys. Rev. Lett. 102 (8) 084302.
[23] R. Mettin, Bubble structures in acoustic cavitation, in: Bubble and Particle Dynamics in Acoustic Fields: Modern Trends and Applications, Research Signpost: Kerala, India, 2005, pp. 1–36.
[24] A. Thiemann, T. Nowak, R. Mettin, F. Holsteyns, A. Lippert, Characterization of an acoustic cavitation bubble structure at 230khz, Ultrason. Sonochemistry 18 (2) (2011) 595–600.
[25] H. Chen, X. Li, M. Wan, S. Wang, High-speed observation of cavitation bubble cloud structures in the focal region of a 1.2MHz high-intensity focused ultrasound transducer, Ultrason. Sonochemistry 14 (3) (2007) 291–297.
[26] L. Biasiori-Poulanges, C. Bourquard, B. Lukić, L. Broche, O. Supponen, Synchrotron X-ray imaging of the onset of ultrasonic horn cavitation, Ultrason. Sonochemistry 92 (2023) 106286.
[27] F. Soulez, L. Denis, C. Fournier, É. Thiébaut, C. Goepfert, Inverse-problem approach for particle digital holography: accurate location based on local optimization, J. Opt. Soc. Amer. A 24 (4) (2007) 1164–1171.
[28] F. Lamadie, L. Bruel, M. Himbert, Digital holographic measurement of liquid–liquid two-phase flows, Opt. Lasers Eng. 50 (12) (2012) 1716–1725.
[29] M. Seifi, C. Fournier, N. Grosjean, L. Mèès, J.-L. Marié, L. Denis, Accurate 3D tracking and size measurement of evaporating droplets using in-line digital holography and "inverse problems" reconstruction approach, Opt. Express 21 (23) (2013) 27964–27980.
[30] L. Mèès, N. Grosjean, J.L. Marié, C. Fournier, Statistical Lagrangian evaporation rate of droplets released in a homogeneous quasi-isotropic turbulence, Phys. Rev. Fluids 5 (11) (2020) 113602.
[31] L. Tian, N. Loomis, J.A. Domínguez-Caballero, G. Barbastathis, Quantitative measurement of size and three-dimensional position of fast-moving bubbles in air-water mixture flows using digital holography, Appl. Opt. 49 (9) (2010) 1549–1554.
[32] Y. Lu, J. Katz, A. Prosperetti, Dynamics of cavitation clouds within a high-intensity focused ultrasonic beam, Phys. Fluids 25 (7) (2013) 073301.
[33] V. Bjerknes, Field of Forces, Col. Univ. Press, New York, 1906.
[34] A.I. Eller, Force on a bubble in a standing acoustic wave, J. Acoust. Soc. Am. 43 (1) (1968) 170–171.
[35] L. Crum, Bjerknes forces on bubbles in a stationary sound field, J. Acoust. Soc. Am. 57 (6) (1975) 1363–1370.
[36] M. Minnaert, On musical air-bubbles and the sounds of running water, Lond. Edinb. Dublin Philos. Mag. J. Sci. 16 (104) (1933) 235–248.
[37] J.-L. Marié, T. Tronchin, N. Grosjean, L. Mèès, O. Öztürk, C. Fournier, B. Barbier, M. Lance, Digital holographic measurement of the Lagrangian evaporation rate of droplets dispersing in a homogeneous isotropic turbulence, Exp. Fluids 58 (2) (2017) 1–13.
[38] A. Francescutto, R. Nabergoj, Pulsation amplitude threshold for surface waves on oscillating bubbles, Acta Acust. United Acust. 41 (3) (1978) 215–220.
[39] P.S. Epstein, M.S. Plesset, On the stability of gas bubbles in liquid-gas solutions, J. Chem. Phys. 18 (11) (1950) 1505–1509.
[40] R. Clift, J.R. Grace, M.E. Weber, Bubbles, Drops, and Particles, Academic Press, New York, 1978.
[41] V.G. Levich, Physical Hydrodynamics, Prentice-Hall, New Jersey, 1962.
[42] J. Magnaudet, D. Legendre, The viscous drag force on a spherical bubble with a time-dependent radius, Phys. Fluids 10 (3) (1998) 550–554.
[43] I.S. Kang, L.G. Leal, The drag coefficient for a spherical bubble in a uniform streaming flow, Phys. Fluids 31 (2) (1988) 233–237.
[44] R. Comolet, Sur le mouvement d'une bulle de gaz dans un liquide, Houille Blanche (1) (1979) 31–42.
[45] S. Cleve, M. Guédra, C. Inserra, C. Mauger, P. Blanc-Benon, Surface modes with controlled axisymmetry triggered by bubble coalescence in a high-amplitude acoustic field, Phys. Rev. E 98 (2018) 033115.
[46] M. Ida, A characteristic frequency of two mutually interacting gas bubbles in an acoustic field, Phys. Lett. A 297 (3–4) (2002) 210–217.
[47] A.A. Doinikov, S.T. Zavtrak, On the mutual interaction of two gas bubbles in a sound field, Phys. Fluids 7 (1995) 1923–1930.
[48] G. Regnault, A.A. Doinikov, C. Mauger, P. Blanc-Benon, C. Inserra, Dynamics of two interacting acoustic bubbles at short separation distances, Phys. Fluids 35 (3) (2023) 037116.
[49] J. Jiao, Y. He, K. Yasui, S.E. Kentish, M. Ashokkumar, R. Manasseh, J. Lee, Influence of acoustic pressure and bubble sizes on the coalescence of two contacting bubbles in an acoustic field, Ultrason. Sonochemistry 22 (2015) 70–77.
[50] G. Regnault, C. Mauger, P. Blanc-Benon, C. Inserra, Secondary radiation force between two closely spaced acoustic bubbles, Phys. Rev. E 102 (3) (2020) 031101.